A Multitheragnostic Nanobubble System to Induce Blood–Brain Barrier Disruption with Magnetically Guided Focused Ultrasound

Hsin-Yang Huang, Hao-Li Liu, Po-Hung Hsu, Chih-Sheng Chiang, Chih-Hung Tsai, Huei-Shang Chi, San-Yuan Chen, and You-Yin Chen**

The blood–brain barrier (BBB) is the main bottleneck to delivering therapeutic agents to diseased areas of the brain for the treatment of brain tumors or diseases of the central nervous system (CNS). Enhanced focused ultrasound (FUS) has been shown to be a successful non-invasive approach[1] to inducing local and reversible BBB disruption in the presence of microbubbles (MBs),[2,3] but a multifunctional and much highly safe vehicle to facilitate FUS-induced BBB disruption without tissue damage should be a priority. As an alternative to MBs, magnetic guidance combined with nanobubble-assisted FUS exposure to disrupt the BBB may be another strategy to: i) deliver multimodality imaging contrast agents (for both diagnostic ultrasound (US) and magnetic resonance imaging), ii) catalyze safe BBB disruption, and iii) deliver drugs via carriers for efficacious therapy of brain disease treatments.

Recently, Ting et al.[4] designed lipid-based MBs loaded with carmustine (bis-chloroethylnitrosourea) (BCNU) and used them to achieve FUS–BBB disruption and local drug delivery in brain glioma treatment. Albumin shell-based MBs have also been used as drug-releasing catalysts, drug carriers, and contrast enhancement agents under FUS-induced therapeutic drug delivery.[5] However, the micrometer-scaled MBs reported in the literature generally have relatively low stability and could potentially damage the endothelium or parenchyma due to their violent cavitation activity when triggered by FUS[6] (such as large-scale erythrocyte extravasations[3]). Furthermore, there is little available information on increasing the safety of FUS–BBB disruption.

Sub-micrometer bubbles or nanobubbles (MNBs) have been used as US contrast agents for imaging and therapy because they can penetrate tumor blood vessel pores for targeted imaging.[7] MNBs intrinsically provide a relatively low US scattering efficiency in comparison to micrometer-sized bubbles, making it difficult to induce enough acoustic cavitation activity to successfully disrupt the BBB.[8] Recently, there have been efforts to develop new structured bubbles to promote microstreaming and enhance the endothelium permeability[9] or to locally increase bubble concentration to produce sufficient activity cavitation.[10] It is still very challenging to use nanometer-sized bubbles to induce BBB disruption with minimal damage to brain tissue in vivo. We therefore hypothesized that by designing novel magnetically guidable (MG) MNBs and employing magnetic guidance to actively increase the local nanobubble concentration, it may enable successful BBB disruption for secure brain drug delivery or therapy. In this study, we synthesized MG theranostic MNBs with dual-modality contrast to concurrently perform FUS-induced BBB disruption and MRI/US dual-modality contrast agent imaging by embedding the super-paramagnetic iron oxide (SPIO) nanoparticles in a silica shell in MNBs.

As illustrated in **Scheme 1**, the proposed MNBs have the potential to become effective US contrast agents and excellent MR susceptibility contrast agents. Interestingly, this is distinct from previous reports[11] on BBB disruption with lipid-based and micrometer-sized bubbles instead of the proposed magnetically silica-based nanometer-sized bubbles. A key feature in this case is the double-targeting scenario; MNBs are first magnetically guided to the nontarget side by an external magnetic field and then FUS exposure is used to locally disrupt the targeted BBB. The accumulated MNBs can increase the BBB disruption efficiency and enhance both US and MR imaging contrast intensity through accumulated MG-guided MNBs.

Figure 1 illustrates the synthesis process for MNBs. We fabricated the bubble agents with a monodispersed distribution to provide maximum excitation efficiency. Polystyrene (PS) particles were used as a core template to form the sub-micrometer-sized MNBs. To adjust the shell properties, including the shell stiffness, porosity, and hydrophilicity, octyltriethoxysilane (OTES), tetraethyl orthosilicate (TEOS), and (3-aminopropyl) triethoxysilane (APTES) were used (Figure 1a). First, the attachment of OTES to the SPIO surface through the organic affinity from the oleic acid conjugation was the key step to modify the surface charge, leading to OTES-modified SPIO nanoparticles that can be easily electrostatically attached to the positively charged PS core particles (shown in Figure 1b). The zeta potential of the OTES-modified SPIO nanoparticles was measured

Dr. H.-Y. Huang, Dr. C.-S. Chiang, H.-S. Chi, Prof. S.-Y. Chen
Department of Materials Science and Engineering
National Chiao Tung University
No. 1001 Ta-Hsueh Rd., Taiwan, Hsinchu 300, Republic of China
E-mail: sanyuanchen@mail.nctu.edu.tw
Prof. H.-L. Liu, Dr. P.-H. Hsu, C.-H. Tsai
Department of Electrical Engineering
Chang Gung University
Tao-Yuan, Taiwan, Republic of China
Prof. Y.-Y. Chen
Department of Biomedical Engineering
National Yang Ming University
No. 155 Sec. 2, Linong St., Taipei, Taiwan 112, Republic of China
E-mail: irradiance@so-net.net.tw

DOI: 10.1002/adma.201403889

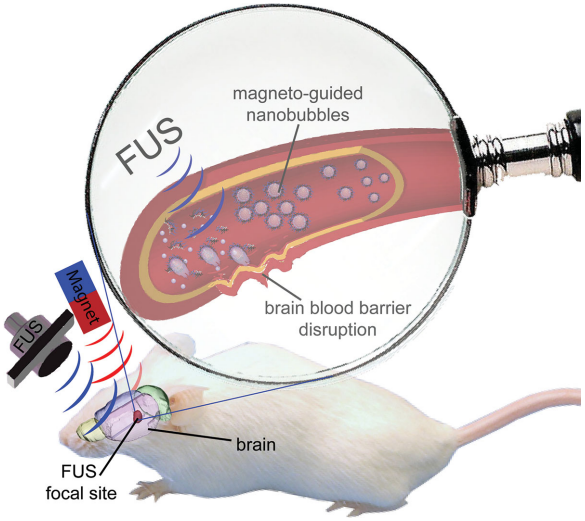

Scheme 1. Schematic diagram of the experimental setup to demonstrate the concept of disrupting the blood–brain barrier (BBB) with the locally accumulated magnetically guidable theranostic nanobubbles (MNBs) in a specific brain area after applying magnetic guidance (MG) in vivo and the local accumulation of MNBs in the vasculature to perform dual targeting of the BBB disruption.

(described in the Supporting Information). Subsequently, TEOS and APTES were added and polymerized in the OTES-modified SPIO-coated PS solution at a pH higher than 11. The former was constructed to form the matrix of the MNB shell and the latter was employed to modify the MNB surface to increase hydrophilic affinity. During the synthesis, the shell thickness can be modulated by changing the TEOS concentration or the reaction time. This is very important because the presence of a shell will impede the oscillation of the bubble, so a thin shell thickness is required to sufficiently stabilize the bubble without impeding the resonance. The core–shell nanoparticle was formed as depicted in Figure 1c. After treatment with tetrahydrofuran (THF) to dissolve the PS core overnight, a hollow structure remained, as shown in Figure 1d. Meanwhile, SPIO particles were embedded in the MNB shell to act as a MR image contrast agent and to enable MG. Because the OTES-modified SPIO interfered in TEOS polymerization to initiate heterogeneous nucleation and growth (discussed later), the porous structures in the silica shell were observed as shown in Figure 1e and in the corresponding enlarged transmission electron microscopy (TEM) image shown in Figure S1 (Supporting Information). A detailed conceptual schematic is shown in Figure 1f, illustrating how the OTES surrounds the SPIO and reacts with TEOS. The OTES was very compatible with the oleic acid-coated SPIO to form a hydrophobic surface that could easily polymerize with TEOS to deposit the silica shell onto the PS core.

To embed SPIO in the shell and modify the shell properties (including roughness and porosity), different OTES concentrations were tested (0, 1.61, 3.22, 4.82, and 6.43 mM). This allowed investigation into the dependence of MNB morphology on the concentration of SPIO (0.3 mM) and TEOS (3.26 mM) during the synthesis process (Figure S2, Supporting Information). Moreover, the addition of SPIO also affected the formation of the MNBs (detailed analysis of the SPIO concentrations on MNB shell formation is described inSupporting Information and shown in Figure S3, Supporting Information. The optimal concentrations of SPIO and OTES were 0.3 and 4.82 mM, respectively, providing sufficient magnetization and creating well-dispersed MNBs in water solution. To investigate the effect of TEOS concentrations on the shell formation of a MNB, we synthesized MNB-1, MNB-2, and MNB-3 with the TEOS concentrations of 3.26, 2.45, and 1.63 mM, respectively.

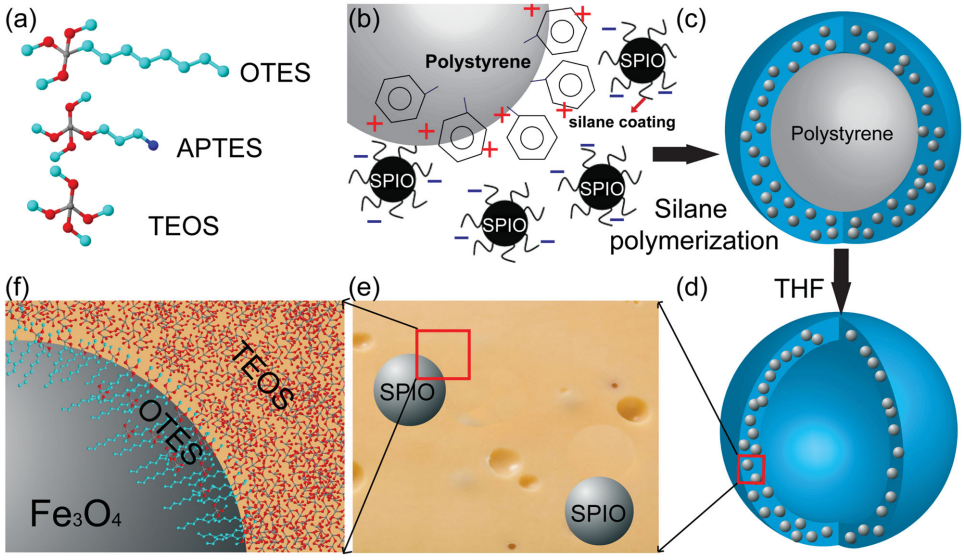

Figure 1. The schematic drawing illustrates the synthesis of MNBs and the interfacial structure of the SPIO/silica. a) The fabrication procedure involved a mixture of silane monomers of TEOS, OTES, and APTES. b) Monodispersed positively charged PS particles were mixed with negatively charged SPIO, and then c) a silica shell was grown onto the PS core particles and mixed with SPIO nanoparticles. d) Hollow MNBs formed after treatment with THF overnight. e) The silica shell presented as a nanoporous structure with embedded SPIO nanoparticles. f) The OTES was very compatible with the oleic acid-conjugated SPIO and the OTES polymerized with TEOS to form the shell on the PS core.

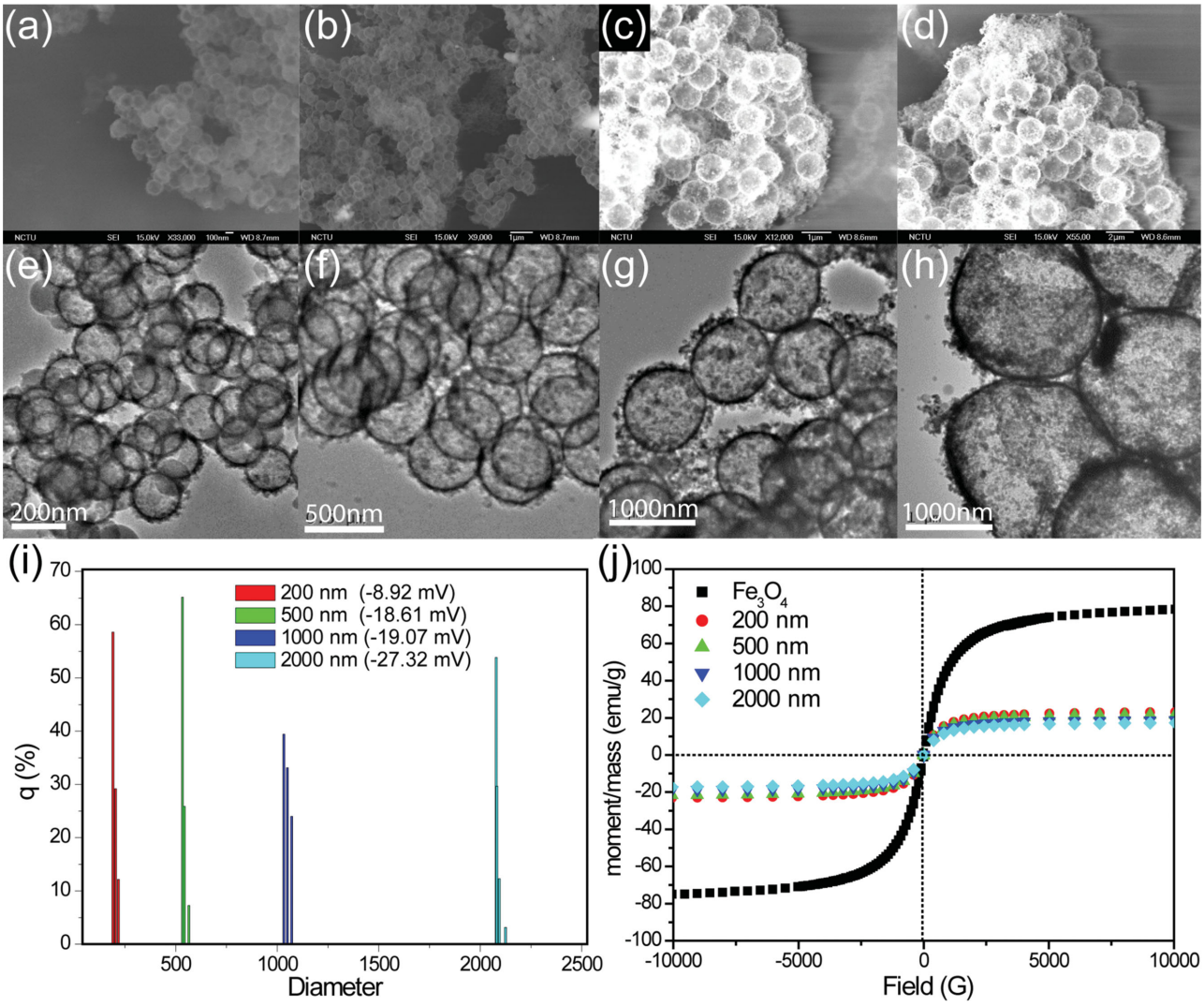

Figure 2. SEM a–d) and TEM e–h) images of MNBs with diameters of 200, 500, 1000, and 2000 nm, respectively. i) The DLS analysis of the monodispersed distributions for different sized MNBs with the zeta potential. j) The measured hysteresis for different sized MNBs showed similar magnetization in the experimental control.

We found that the MNB shell with the highest TEOS concentration (3.26 mM) still retained a spherical bubble shape (Figure S4a, Supporting Information). However, as the TEOS concentration decreased (Figure S4b,c, Supporting Information, from 2.45 to 1.63 mM, respectively), the bubble failed to maintain a perfect spherical bubble due to the weakness of the softer shell under a vacuum condition (i.e., the TEM operation state). Furthermore, we found that no bubble was formed at a TEOS concentration below 0.815 mM because it was not easy to form a cross-linked shell around the PS core with a lower TEOS concentration (Figure S5, Supporting Information). Using a TEOS concentration higher than 1.63 mM to polymerize with OTES on the PS core, the bubble structure more stably formed when compared with bubbles formed under lower TEOS concentrations (described in Supporting Information). After FUS exposure, the shell morphology of MNB-1 slightly changed as shown in the TEM image (Figure S4d, Supporting Information), whereas MNB-2 and MNB-3 showed evident bubble collapse and fragmentation (Figure S4e,f, Supporting Information). For BBB disruption with FUS exposure, the MNBs responded to FUS energy by oscillating or collapsing, which resulted in high-acoustic emissions that produce shear streams to stimulate endothelial/tight junction structure.[12]

Therefore, given the abovementioned results, we further synthesized MNBs of different sizes from sub-micrometer to micrometer scale, with similar shell thicknesses, in the following in vitro and in vivo experiments (**Figure 2**). The corresponding scanning electron microscopy (SEM) and TEM images of MNBs with sizes of 200, 500, 1000, and 2000 nm are shown in Figure 2a–d and e–h, respectively. All of the MNBs displayed monodispersed particle distribution. These monodispersed images were consistent with the dynamic laser scanning (DLS) data (Figure 2i), and the negative surface charge increased with increasing SPIO particle content on the surface. A superconducting quantum interference device (SQUID) was employed to measure the magnetic hysteresis

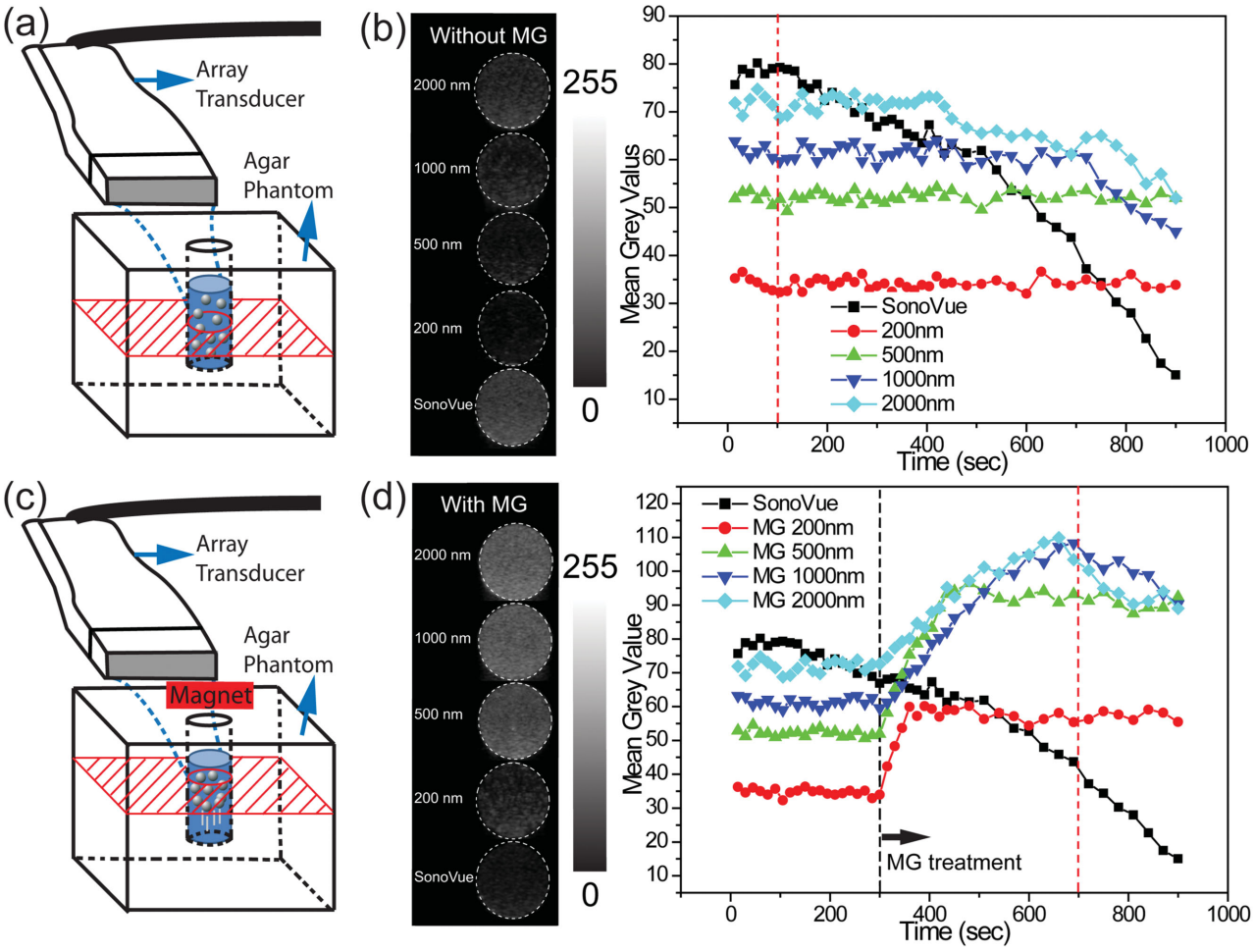

Figure 3. a) Schematic diagram of the experimental setup of the dynamic US B-scan and the comparison of US image intensity with different sized MNBs and SonoVue over time. b) US images with MNBs and SonoVue at $t = 100$ s. The stronger intensity of US images from the SonoVue bubble compared with those from MNBs in the initial phases of scanning ($t = 0$–200 s). Slow or no decay of the signal intensities of MNBs were compared with those of SonoVue. c) Schematic diagram of the experimental setup to investigate the changes in US image intensity with different sized MNBs and SonoVue before/after receiving MG. Following MG, a magnet was put on the surface of an agarose cubic phantom 1 cm from the liquid surface of the sample. d) US images with MNBs and SonoVue at $t = 700$ s (400 s postMG). There was a significant increase in signal intensity of MNBs after receiving MG, while SonoVue presented gradual signal decay over time.

(emu/MNB weight) of the MNBs, showing similar magnetization and hysteresis characteristics among the various sized MNBs (Figure 2j). This implies that a similar SPIO concentration embedded in the shell of the MNBs dominates the magnetization of MNB, and is less dependent on MNB size.

We observed that MNBs can provide acoustic emission cavitation activity with FUS exposure that is comparable to that of commercial lipid-based MBs from SonoVue. SonoVue under US exposure simultaneously triggers both harmonic (or called stable) and wideband (or so-called inertial) emissions and is dependent on the US exposure power level. In contrast, the MNBs were superior at triggering harmonic cavitation activity only (for example, 10–15 W for 500 nm MNBs) (Figure S6, Supporting Information). When combined with MG, the acoustic emission of MNBs can be further enhanced significantly (Figure S7, Supporting Information). This supports the synergetic use of MG and US exposure with MNBs to facilitate harmonic-only acoustic emission cavitation activity.

Figure 3a shows the comparison of US imaging contrast changes tested in vitro among the 2000, 1000, 500, 200 nm MNBs and SonoVue. After investigating the temporal behavior of the US contrast intensity for each sample, we analyzed differences in the time–intensity curve (TIC) generated by four different-sized MNBs and SonoVue bubbles without MG (Figure 3b). The typical US phantom images of the four different sized MNBs and SonoVue at 100 s (red dotted line) are also shown in Figure 3b. We noted that the TIC measured for SonoVue bubbles was a higher intensity in the initial phase (<200 s) than that measured for MNBs, and that the intensity increased with MNB bubble size. However, it was also observed that the intensity of TICs was more attenuated as time increased with SonoVue than with micrometer-scaled bubbles (2000 and 1000 nm MNBs), indicating less diffusion of gases from the solid shell of the MNB. In a comparison of different MNB sizes, the increased bubble size produced larger intensity attenuation in the TIC because it is easier to destroy a

micrometer-scaled bubble than a sub-micrometer-scaled bubble (the larger the bubble size, the better the ultrasonic response). Consequently, this leads to shell fragmentation and easy bubble liberation, causing gas to dissolve into the surrounding host fluid over time.[13] On the other hand, the structural stability of smaller sized MNBs is greater than that of larger sized MNBs because of the same shell thickness prerequisite. Regarding signal intensity changes in sub-micrometer-scaled bubbles (500 and 200 nm) over a longer period of time from US imaging, we did not observe an evident decrease in signal intensity over the 15 min observation duration because of the stable shell structure of sub-micrometer-scaled MNBs. When comparing 500 and 200 nm MNBs, only the 500 nm MNBs provided sufficient satisfactory signal intensity.

The enhancement of US imaging contrast following MG was further investigated using the same experimental setup for imaging US phantoms described in the above section (Figure 3c). After 300 s of continuous US imaging of the phantom, the magnet was placed adjacent to the phantom to provide MG guidance of MNBs. Applying MG induced significant MNB accumulation, enhancing the increase in US imaging contrast intensity (Figure 3d). The TICs for different sized MNBs before/after receiving MG, and the typical US phantom images at 700 s (red dotted line) are also displayed. Following MG with micrometer-scaled MNBs, we observed an enhanced intensity of US imaging. TICs measured for micrometer scale MNBs revealed an initial increase followed by a final decrease caused by outward diffusion of the gas from the MNBs due to instability and destruction of the MNBs. The peaks of TICs measured for both 2000 and 1000 nm MNBs were at 400 s postMG. Compared with the US imaging intensities for 2000 and 1000 nm MNBs before receiving MG, the enhancements were quantified as 1.49- and 1.73-fold increases, respectively. Following MG on sub-micrometer-scaled MNBs, higher rise rates of TIC were observed compared with those of micrometer-scaled MNBs. TICs measured for 500 and 200 nm MNBs reached plateaus at 100 and 150 s postMG, respectively, and were then sustained over the experimental time. The intensities of US imaging with 500 and 200 nm MNBs + MG showed 1.88- and 1.92-fold increases, respectively, compared with those before MG. Because the TIC measured for SonoVue bubbles revealed gradual decay without magnetic influence, the TICs measured at micrometer-scaled MNBs and the TIC measured at 500 nm MNBs were higher than those measured for SonoVue after receiving MG for 100 s. Interestingly, we noted that the intensity of US imaging for 500 nm MNBs post MG was significantly higher than that for SonoVue bubbles in the initial US imaging phase.

Next, we examined the feasibility of combining MG/FUS exposure (Figure S8a, Supporting Information) and MNB-2 administration to locally and transiently open the BBB. First, the dependence of FUS–BBB disruption on MNB size was investigated. MNB-facilitated FUS exposure can successfully induce local BBB disruption without the application of MG when micrometer-sized MNBs (1000 and 2000 nm) were administered (60 μL, 10 mg mL^{-1}), as confirmed by the Evans blue (EB) dye extravasations into the brain parenchyma (Figure S8b, Supporting Information). The 500 and 200 nm MNBs without MG failed to induce the same BBB-disruption effect (Figure S8b, Supporting Information) due to their sub-micrometer size, which produces insufficient acoustic emissions to stimulate capillary basal lumens. The limiting factor in using sub-micrometer MNBs in FUS exposure to disrupt the BBB can be overcome when MG is applied because it creates a high concentration of MNBs and FUS-targeted positions and is capable of producing sufficiently high acoustic emissions. The 500 nm MNBs (60 μL, 10 mg mL^{-1}) were administered with a combination of FUS exposure and MG treatment. An aerial view of an animal brain reveals that a FUS-induced BBB disruption can be produced with the introduction of MG (Figure S8c, Supporting Information).

In a series test, we observed that even when applying MG, the 200 nm MNBs still cannot provide a successful BBB disruption with FUS. Possible explanations include the abovementioned small size, which fails to provide sufficient acoustic emissions on the adjacent capillary lumens even when MG is applied to significantly increase local MNB concentrations. Additionally, higher acoustic pressure is necessary to provide an equivalent cavitation scale when decreasing the MNB dimension.

Moreover, we employed in vivo T_2*-MRI to observe the MNB distribution and evaluate correlations with brain tissue histology. Again, for administration of 500 nm MNBs without MG, no apparent change was observed in the brain histology (EB dye leakage) or T_2*-MRI (no dark signal in brain tissue, **Figure 4**a). In contrast, when applied with MG, both the brain tissue sections and the T_2*-MRI confirmed the disruption of the BBB based on the EB penetration and the MNB deposition (dark signal in brain tissue, Figure 4b). The T_2*-MRI also showed a high correlation between the hyposignal distribution (caused by the SPIO embedded in the MNBs) and the distribution of the high EB leakage regions.

It is also worth noting that the application of MRI provides validation of the BBB disruption and the MNB distributions (provided by hyposignal distribution from T_2* images). Overall, using the MRI monitoring and the intrinsic theranostic feature of MNBs to facilitate FUS-induced BBB disruption and local drug delivery for potential brain tumors and CNS disorders might prove useful with a combination of MNBs and MG. Furthermore, the high correlation between the hyposignal distribution and the EB leakage regions indicate that the developed MNBs would be helpful in the diagnosis of brain disorders by MRI without the need for animal sacrifice or animal tissue section work. Moreover, to our knowledge, the 500 nm MNBs are the first sub-micrometer-scaled bubbles for FUS-induced BBB disruption.

Under FUS treatment, acoustic emissions can be triggered much more easily and more profoundly via a larger bubble size,[14] yet the overwhelming cavitation energy induced by large-bubble violent collapse or explosion during FUS exposure can easily produce strong microjets that damage endothelial cells or CNS tissue. Therefore, we further investigated the relationship between spatial MRI contrast enhancement and the pathological events of FUS-induced BBB disruption in vivo with different MNB sizes. The laboratory-designed MNBs were used as the MRI contrast agent to quantitatively assess the area of the BBB disruption. Meanwhile, the histological analysis using hematoxylin and eosin (H&E) stain was performed to examine the presence of hemorrhaging or brain tissue damage caused

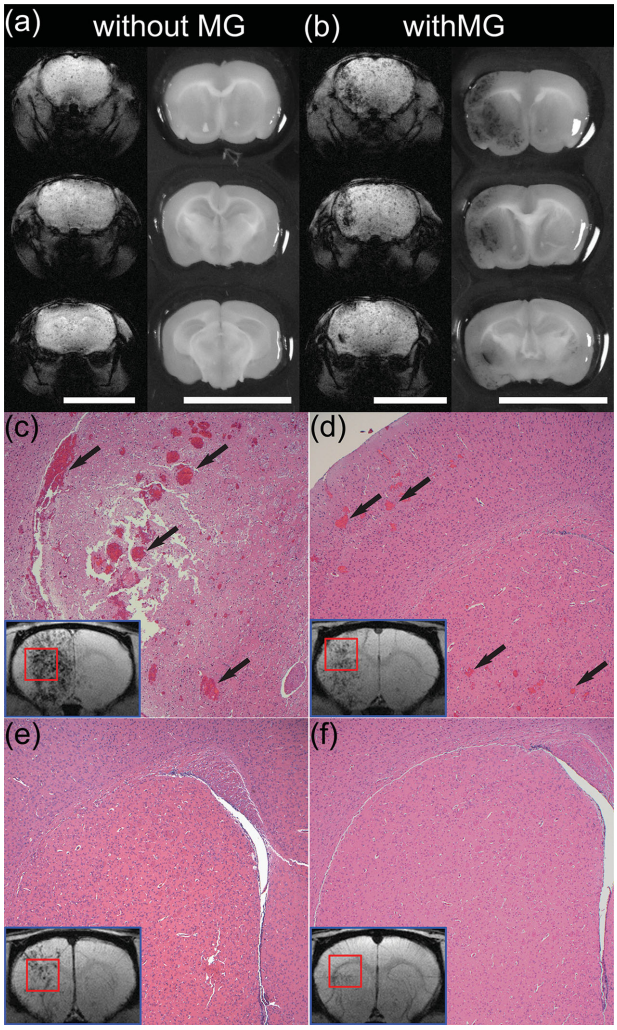

Figure 4. a) Representative images of T_2* gradient echo coronal sections and their corresponding EB dye-stained in wet brain tissue slices to evaluate the efficiency of MG on 500 nm MNB-assisted FUS-BBB disruption. BBB disruption was confirmed both from brain sections (with EB dye leakage) and MRI (with MNBs) with MG against those without MG (scale bar = 1 cm). b) The comparison of the biological safety for FUS-induced BBB disruption in vivo with different MNB sizes. Representative T_2*-MRI sections and their corresponding H&E stained slices were used to investigate the BBB permeability and hemorrhagic damage from c) MG-assisted FUS-exposure with 2000 nm MNBs. There was major tissue destruction and hemorrhage (arrowed) found in the mouse striatum where SPIO-embedded MNBs had diffused, and obvious contrast enhancement was shown. d) MG-assisted FUS-exposure with 1000 nm MNBs. The microhemorrhagic damage (arrowed) was still found in the mouse striatum where the contrast enhancement of T_2*-MRI indicated the altered BBB permeability. e) MG-assisted FUS-exposure with 500 nm MNBs. The contrast enhancement of T_2*-MRI due to MNB diffusion into the area of the sonicated striatum where hemorrhagic damage was found from HE stained slice. f) MG-assisted FUS exposure with 200 nm MNBs. There was neither MRI contrast enhancement nor hemorrhagic damage in the exposure area confirmed by T_2*-MRI imaging and HE histological examination.

by the FUS-induced BBB disruption. A total of 30 (N = 30) mice were used for the purposes of this study, separated into five groups. Each animal was sonicated with various MNB sizes (diameter of 2000, 1000, 500, and 200 nm) and SonoVue at FUS exposure power level of 10 W (equivalent to peak pressure of 1.15 MPa) and a FUS focal spot targeted to the left striatum of animals. Animals also underwent MRI and histology after the MG/FUS exposures.

Regional contrast enhancement on in vivo T_2*-MRI indicated that the permeability of the BBB was altered on the left striatum as a result of the FUS in conjunction with 2000, 1000, and 500 nm MNBs, respectively, as shown in Figure 4c–e. However, cerebral hemorrhage was only detected on the H&E stained slices when the BBB disruption was performed by FUS in conjunction with micrometer-scaled MNBs as shown in Figure 4c–d. The histological analysis (Table S1, Supporting Information) also showed that the occurrence and severity of cerebral hemorrhage increased with increasing MNB diameter, which reached micrometer size. When MG/FUS-induced BBB disruption with the 1000 or 2000 nm MNBs was used, the occurrence of grouped erythrocyte extravasations was similar to or higher than that of SonoVue (occurrence = 55.8% and 83.7% compared with 52.2%, respectively).

When the animal brains were sonicated with the 500 or 200 nm MNBs, rare erythrocyte extravasations occurred as shown by H&E stains (Figure 4e–f). However, on T_2*-MRI contrast, the changes were observed when the animal received the MG/FUS-induced BBB disruption with the 500 nm MNBs (Figure 4e). Meanwhile, the occurrence of erythrocyte extravasations during FUS-induced BBB-disruption in 500 nm MNBs combined with MG was found to be significantly less (occurrence = 9.0%) (Table S1, Supporting Information). This supports the observation that MNBs trigger less wideband acoustic emission (i.e., inertial cavitation) and thus, effectively reduce the tissue and capillary damage induced by bubble collapse. Therefore, taking into account the more efficient BBB disruption and biological safety, the 500 nm MNB may be preferable for further applications.

The use of FUS exposure in the presence of bubbles has been shown to effectively provide acoustic emission to the endothelium and trigger temporal cell deformation to create temporal CNS vascular–parenchyma-enhanced permeability. This creates a new opportunity to overcome BBB blockage and achieve therapeutic molecule delivery into the CNS. New types of lipid-shell submicrometer bubbles (about 800–1100 nm) have been reported in the application of FUS-BBB disruption with the benefit of better tissue hazard control.[15] Also, Chen et al.[16] have reported the use of lipid-shelled acoustically activated nanodroplets with an original size of 200 nm to explore the possibility of BBB disruption. The former requires triggering at a specific matched frequency to avoid lipid bubble collapse, and the latter requires triggering nanodroplets to expand to micrometer scale and induce a sufficiently high acoustic emission. Furthermore, there is always a dilemma when triggering higher acoustic emission while retaining the biosafety of nanometer-sized bubbles. This study presents a novel direction of employing monodispersed silica shelled, perfluoropantane-encapsulated magneto-nanobubbles, and this is the first study to demonstrate successful induction of BBB-disruption via bubble size as small as 500 nm combined with FUS exposure and magnetic guidance.

In summary, we have shown for the first time that a SPIO-doped strategy successfully stabilizes the silica-based shell structure to form a perfluoropantane-encapsulated nanobubble

structure. The MNBs serve as a satisfactory dual-modality contrast agent for both MRI and US imaging. Due to the nanometer size, the proposed MNB can serve as a suitable drug-carrying vehicle to penetrate an abnormal vascular bed for therapy. Of note, we have proven that, in the most challenging CNS drug delivery issue, the MNB can be magnetically guided and used in conjunction with US to open the BBB. Conclusively, the proposed MNB platform has the potential to serve as a unique theranostic tool for multimodality imaging systems, and also is a promising mechanism for improved drug delivery of therapeutic substances or gene therapy into CNS.

Supporting Information

Supporting Information is available from the Wiley Online Library or from the author.

Acknowledgements

H.-Y.H. and H.-L.L. contributed equally to this work. This work was financially supported by the National Science Council of the Republic of China, Taiwan under Contract of NSC100–2320-B-009–006-MY2. This work is also supported by the "Aim for the Top University" program of the National Chiao Tung University and the Ministry of Education, Taiwan, Republic of China. The authors also thank 7T animal MRI Core Lab of the Neurobiology and Cognitive Science Center for technical and facility support and C. H. Hsieh and J. H. Chen of the Instrumentation Center for MRI experiments at the National Taiwan University. The authors are grateful for the 7T animal MRI support of the Molecular Imaging Center, the Chang-Gung Memorial Hospital as well. All the animal experiments were conducted in accordance with the guidelines of the Animal Research Committee of National Yang Ming University and National Chiao Tung University, Taiwan.

Received: August 25, 2014
Published online: December 3, 2014

[1] a) S. Mitragotri, *Nat. Rev. Drug Discovery* **2005**, *4*, 255; b) J. E. Kennedy, *Nat. Rev. Cancer* **2005**, *5*, 321; c) X. Wang, H. Chen, Y. Chen, M. Ma, K. Zhang, F. Li, Y. Zheng, D. Zeng, Q. Wang, J. Shi, *Adv. Mater.* **2012**, *24*, 785; d) D. Niu, X. Wang, Y. Li, Y. Zheng, F. Li, H. Chen, J. Gu, W. Zhao, J. Shi, *Adv. Mater.* **2013**, *25*, 2686.

[2] a) N. Sheikov, N. McDannold, N. Vykhodtseva, F. Jolesz, K. Hynynen, *Ultrasound Med. Biol.* **2004**, *30*, 979; b) J. J. Choi, J. A. Feshitan, B. Baseri, W. Shougang, T. Yao-Sheng, M. A. Borden, E. E. Konofagou, *IEEE Trans. Biomed. Eng.* **2010**, *57*, 145.

[3] S. Meairs, A. Alonso, *Prog. Biophys. Mol. Biol.* **2007**, *93*, 354.

[4] C.-Y. Ting, C.-H. Fan, H.-L. Liu, C.-Y. Huang, H.-Y. Hsieh, T.-C. Yen, K.-C. Wei, C.-K. Yeh, *Biomaterials* **2012**, *33*, 704.

[5] A.-H. Liao, H.-L. Liu, C.-H. Su, M.-Y. Hua, H.-W. Yang, Y.-T. Weng, P.-H. Hsu, S.-M. Huang, S.-Y. Wu, H.-E. Wang, T.-C. Yen, P.-C. Li, *Phys. Med. Biol.* **2012**, *57*, 2787.

[6] M. Schneider, *Echocardiography* **1999**, *16*, 743.

[7] a) T. Yin, P. Wang, J. Li, R. Zheng, B. Zheng, D. Cheng, R. Li, J. Lai, X. Shuai, *Biomaterials* **2013**, *34*, 4532; b) Z. Xing, J. Wang, H. Ke, B. Zhao, X. Yue, Z. Dai, J. Liu, *Nanotechnology* **2010**, *21*, 145607; c) Y. Wang, X. Li, Y. Zhou, P. Huang, Y. Xu, *Int. J. Pharm.* **2010**, *384*, 148; d) C.-H. Wang, Y.-F. Huang, C.-K. Yeh, *Langmuir* **2011**, *27*, 6971; e) C.-H. Wang, S.-T. Kang, Y.-H. Lee, Y.-L. Luo, Y.-F. Huang, C.-K. Yeh, *Biomaterials* **2012**, *33*, 1939; f) H.-Y. Huang, S.-H. Hu, S.-Y. Hung, C.-S. Chiang, H.-L. Liu, T.-L. Chiu, H.-Y. Lai, Y.-Y. Chen, S.-Y. Chen, *J. Controlled Release* **2013**, *172*, 118.

[8] a) T. L. Zhe Liu, Josef Ehling, Stanley Fokong, Jörg Bornemannc, Fabian Kiessling, Jessica Gätjens, *Biomaterials* **2011**, *32*, 6155; b) F. Yang, Y. Li, Z. Chen, Y. Zhang, J. Wu, N. Gu, *Biomaterials* **2009**, *30*, 3882.

[9] a) A. Xie, T. Belcik, Y. Qi, T. K. Morgan, S. A. Champaneri, S. Taylor, B. P. Davidson, Y. Zhao, A. L. Klibanov, M. A. Kuliszewski, H. Leong-Poi, A. Ammi, J. R. Lindner, *JACC: Cardiovascular Imaging* **2012**, *5*, 1253; b) C.-H. Fan, C.-Y. Ting, H.-L. Liu, C.-Y. Huang, H.-Y. Hsieh, T.-C. Yen, K.-C. Wei, C.-K. Yeh, *Biomaterials* **2013**, *34*, 2142; c) F. M. Kievit, M. Zhang, *Adv. Mater.* **2011**, *23*, H217.

[10] a) E. Y. Lukianova-Hleb, X. Ren, J. A. Zasadzinski, X. Wu, D. O. Lapotko, *Adv. Mater.* **2012**, *24*, 3831; b) R. Suzuki, Y. Oda, N. Utoguchi, K. Maruyama, *J. Controlled Release* **2011**, *149*, 36; c) J. M. Warram, A. G. Sorace, R. Saini, H. R. Umphrey, K. R. Zinn, K. Hoyt, *J. Ultrasound Med.* **2011**, *30*, 921.

[11] a) K. Hynynen, N. McDannold, N. Vykhodtseva, F. A. Jolesz, *Radiology* **2001**, *220*, 640; b) K. Hynynen, N. McDannold, N. Vykhodtseva, F. A. Jolesz, *Acta Neurochir. Suppl.* **2003**, *86*, 555; c) H. L. Liu, Y. Y. Wai, W. S. Chen, J. C. Chen, P. H. Hsu, X. Y. Wu, W. C. Huang, T. C. Yen, J. J. Wang, *Ultrasound Med. Biol.* **2008**, *34*, 598.

[12] a) H. Chen, A. A. Brayman, W. Kreider, M. R. Bailey, T. J. Matula, *Ultrasound Med. Biol.* **2011**, *37*, 2139; b) H. Chen, W. Kreider, A. A. Brayman, M. R. Bailey, T. J. Matula, *Phys. Rev. Lett.* **2011**, *106*, 034301.

[13] J. E. Chomas, P. Dayton, J. Allen, K. Morgan, K. W. Ferrara, *IEEE Trans. Ultrason. Ferroelectr. Freq. Control* **2001**, *48*, 232.

[14] a) E. P. Stride, C. C. Coussios, *Proc. Inst. Mech. Eng., Part H* **2010**, *224*, 171; b) E.-A. Brujan, *Microfluid. Nanofluid.* **2011**, *11*, 511; c) E. G. Schutt, D. H. Klein, R. M. Mattrey, J. G. Riess, *Angew. Chem. Int. Ed.* **2003**, *42*, 3218.

[15] C. H. Fan, H. L. Liu, C. Y. Ting, Y. H. Lee, C. Y. Huang, Y. J. Ma, K. C. Wei, T. C. Yen, C. K. Yeh, *PLoS ONE* **2014**, *9*, e96327.

[16] C. C. Chen, P. S. Sheeran, S. Y. Wu, O. O. Olumolade, P. A. Dayton, E. E. Konofagou, *J. Controlled Release* **2013**, *172*, 795.